Direct propylene epoxidation with oxygen using a photo-electro-heterogeneous catalytic system

Myohwa Ko[1,2,6], Yongseon Kim[1,2,6], Jinwoo Woo[1,6], Boreum Lee[1], Rashmi Mehrotra[1,2], Pankaj Sharma[1,2], Jinjong Kim[3], Seon Woo Hwang[1,2], Hu Young Jeong[4], Hankwon Lim[1,2], Sang Hoon Joo[3] ✉, Ji-Wook Jang[1,2,5] ✉ and Ja Hun Kwak[1,2] ✉

Propylene oxide is a crucial feedstock in the plastic industry. The direct epoxidation of propylene using O_2 is considered among the most promising means of producing propylene oxide. Here we report an integrated photo-electro-heterogeneous catalytic system for propylene epoxidation with O_2. Bismuth vanadate (or TiO_2) photocatalyst and a Co-based electrocatalyst produces H_2O_2. A titanium silicalite-1 heterogeneous catalyst subsequently epoxidizes propylene to propylene oxide with the in situ-generated H_2O_2. The proposed system enables propylene oxide production with O_2 as the sole oxidizing agent under light irradiation without using H_2, a sacrificial agent, or external bias. It stably produces propylene oxide for 24 h with high selectiv-ity (≥98%) under ambient conditions. These results demonstrate the potential of this catalytic system to produce chemical compounds in an environmentally benign manner.

Propylene oxide (PO) constitutes one of the most important feedstocks in the plastic industry, which is used to produce polyurethane, polyester and propylene glycol (PG)[1]. Its production exceeds 10 million tonnes per year, and the demand for PO is gradually increasing[2,3]. Most industrial PO has been produced using either a chlorohydrin or hydroperoxide process[4]. However, they require additional complex purification steps due to the generation of large amounts of coproducts and pose environmental risks due to the use of toxic chemicals and production of large volumes of wastewater. Thus, direct epoxidation using O_2, which is a well-established method in ethylene oxide production, is considered the most desirable way to produce PO and has been explored intensively[5–7]. However, unlike ethylene, propylene contains an allylic hydrogen atom, and its abstraction can result in further oxidation[8]. Great efforts have been made to develop a process for the direct synthesis of PO using O_2, but such processes have suffered from low activity and selectivity and thus still remain a challenge[9,10].

Recently, a propylene epoxidation process using hydrogen peroxide (H_2O_2) as an oxidizing agent (hydrogen-peroxide/propylene-oxide, HPPO) has received substantial attention because this process shows high PO selectivity (>95%) and generates water as the only coproduct[11]. The HPPO process itself is environmentally benign; however, current H_2O_2 production through the anthraquinone process involves multistep reactions and produces large volumes of organic waste[12]. Alternatively, PO production methods using in situ-generated H_2O_2 have been developed. For example, Haruta et al. used Au supported on titanium oxides, wherein H_2O_2 was synthesized from H_2 with O_2 on Au and reacted with propylene at nearby Ti^{4+} sites to produce PO[13]. Although this process proceeds in a single reaction system, it suffers from unavoidable safety problems and rapid catalyst deactivation[14,15]. To date, to the best of our knowledge, no approaches have been successful in producing PO using O_2 as the only oxidizing agent.

In this study, we developed an integrated photo-electro-heterogeneous catalytic system by coupling photo-electrochemical H_2O_2 production and propylene epoxidation using in situ-generated H_2O_2 over a heterogeneous zeolite catalyst. This system is composed of a nanostructured photocatalyst (bismuth vanadate ($BiVO_4$) or TiO_2), an electrocatalyst comprising atomically dispersed Co–N_x sites on carbon nanotubes (Co–N/CNT) and a heterogeneous catalyst based on titanium silicalite-1 (TS-1). It enables the direct epoxidation of propylene using O_2 under light irradiation without any H_2, sacrificial agent or electrical energy under ambient conditions. This system allows for the stable production of PO over 24 h with high selectivity (≥98%) under simulated solar and visible light illumination.

Results

Photo-electro-heterogeneous catalytic system. To perform propylene epoxidation using O_2, the overall reaction should be performed by three catalysts—a photocatalyst for photovoltage generation, an electrocatalyst for selective O_2 reduction to H_2O_2 and a heterogeneous catalyst for propylene epoxidation with in situ-generated H_2O_2 (Fig. 1). When a semiconductor photocatalyst receives solar energy, photoexcitation generates charge carriers; the photogenerated hole in the valence band oxidizes water to O_2, and the electrons move towards the electrocatalyst, which selectively reduces O_2 to H_2O_2. The heterogeneous catalyst then epoxidizes propylene to PO using in situ H_2O_2 as an oxidizing agent. In this way, the catalytic system can produce PO from propylene, O_2 and solar energy without any additional bias or expensive chemicals, making it a straightforward (one-pot), energy-saving (O_2 as a reactant without

[1]School of Energy and Chemical Engineering, Ulsan National Institute of Science and Technology (UNIST), Ulsan, Republic of Korea. [2]Department of Energy Engineering, Ulsan National Institute of Science and Technology (UNIST), Ulsan, Republic of Korea. [3]Department of Chemistry, Ulsan National Institute of Science and Technology (UNIST), Ulsan, Republic of Korea. [4]Graduate School of Semiconductor Materials and Devices Engineering, Ulsan National Institute of Science and Technology (UNIST), Ulsan, Republic of Korea. [5]Emergent Hydrogen Technology R&D Center, Ulsan National Institute of Science and Technology (UNIST), Ulsan, Republic of Korea. [6]These authors contributed equally: Myohwa Ko, Yongseon Kim, Jinwoo Woo.

✉e-mail: shjoo@unist.ac.kr; jiwjang@unist.ac.kr; jhkwak@unist.ac.kr

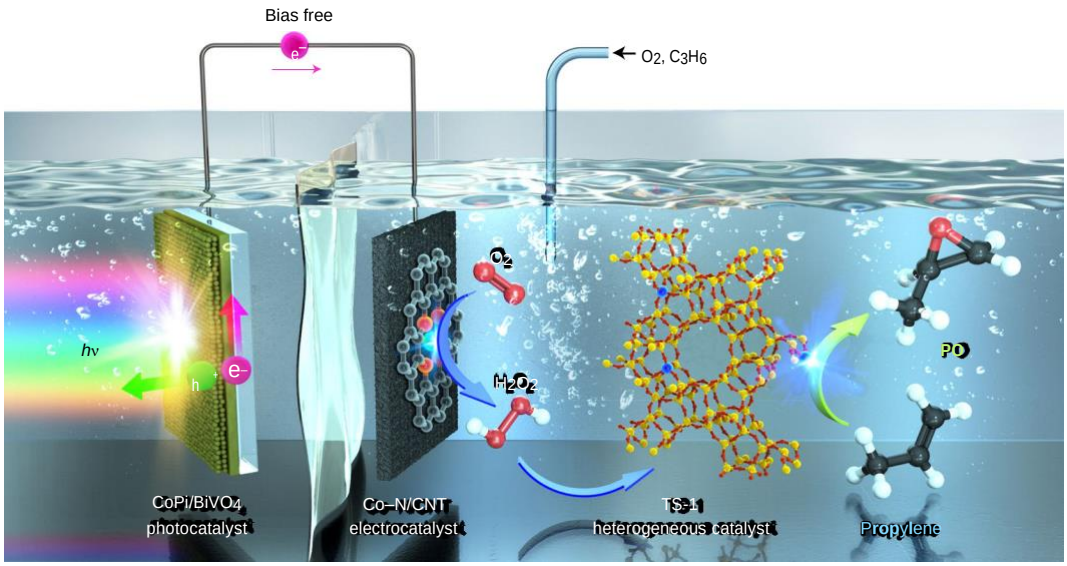

Fig. 1 | Schematic of PO production in photo-electro-heterogeneous catalytic system. The CoPi/$BiVO_4$ (cobalt-phosphate-loaded bismuth vanadate) photocatalyst promotes water oxidation under light illumination, and the Co–N/CNT electrocatalyst carries out continuous O_2 reduction to H_2O_2. A Nafion proton exchange membrane separates the anodic and cathodic parts of the photo-electrochemical cell. TS-1 heterogeneous catalyst continuously epoxidizes propylene to PO by using in situ-generated H_2O_2 as an oxidizing agent.

a need for electrical energy) and environmentally benign (no toxic chemicals or harmful coproducts) process.

Catalyst characterization. As a photoanode for oxidizing water, a rutile TiO_2 nanowire film was employed. The nanowire TiO_2 was hydrothermally grown on a fluorine-doped tin oxide (FTO) glass substrate[16,17]. The X-ray diffraction pattern of TiO_2 showed diffraction peaks at 36.1°, 41.2° and 62.8°, which is commensurate with the rutile TiO_2 phase (Fig. 2a). A homogeneous TiO_2 film, consisting of vertically aligned, 100- to 200-nm-diameter nanowire arrays, was observed with scanning electron microscopy (SEM) imaging (Fig. 2b). High-resolution transmission electron microscopy (HR-TEM) images revealed that the TiO_2 nanowire grew along the [001] direction, with lattice fringes having interplanar spacings of 0.32 and 0.29 nm, consistent with the lattice spacings (*d* spacings) of the (110) and (001) planes of rutile TiO_2, respectively (Fig. 2b inset)[18].

As a second photoanode, $BiVO_4$ film was fabricated onto FTO following a two-step synthesis method involving electrodeposition of bismuth oxyiodide (BiOI), followed by thermal treatment in the presence of vanadium salt[19]. X-ray diffraction patterns revealed that BiOI was prepared as a pure phase and that it was successfully converted to monoclinic $BiVO_4$ (Fig. 2c and Supplementary Fig. 1). X-ray photoelectron spectroscopy (XPS) analysis indicated that no iodide was present within the detection level in the $BiVO_4$ film (Supplementary Fig. 2a). Subsequently, cobalt phosphate (CoPi), as an oxygen evolution catalyst, was photo-electrochemically deposited onto the $BiVO_4$ film to promote the kinetics of water oxidation and improve the stability of bare $BiVO_4$, which possesses poor catalytic properties[20,21]. The formation of CoPi was verified using XPS (Supplementary Figs. 2b,c). The top- and side-view SEM images of CoPi/$BiVO_4$ with N_2 adsorption–desorption isotherm measure-ments showed that $BiVO_4$ particles (diameter, 150–250 nm) were closely interconnected, generating macroporous structures with a uniform thickness of 1.2 μm (Fig. 2d and Supplementary Figs. 3 and 4). The optical bandgap for the macroporous CoPi/$BiVO_4$ film was estimated to be ~2.57 eV (Tauc plot; Supplementary Fig. 5).

A Co–N/CNT catalyst was used to selectively reduce O_2 to H_2O_2. The Co–N/CNT catalyst was prepared using 5,10,15,20-tetrakis(4-methoxyphenyl)-21*H*,23*H*-porphine cobalt(II) (CoTMPP) as the precursor, following previously reported protocols with slight modification[22]. Structural information on the Co–N/CNT was obtained via extended X-ray absorption fine structure (EXAFS) spectral analyses (Fig. 2e). The radial distribution function of the Fourier-transformed (FT) EXAFS spectra of the CoTMPP reference showed a major peak at 1.45 Å corresponding to the Co–N coordination. A major peak from the Co foil appeared at 2.15 Å, which could be attributed to the Co– Co metallic bonding. The EXAFS spectrum of Co–N/CNT exhib-ited a peak only at 1.45 Å, indicating that Co–N/CNT comprises Co–N/O bonds without agglomerated Co particles. The high-angle annular dark-field scanning TEM (HAADF-STEM) image of the Co–N/CNT (Fig. 2f) shows tiny white dots, indicating the forma-tion of atomically dispersed Co–N_x sites on CNT. The X-ray dif-fraction pattern for the Co–N/CNT catalyst showed only broad diffraction peaks near 26°, 43° and 53°, which originate from the acid-treated CNT support, confirming the absence of Co particles (Supplementary Fig. 6).

For propylene epoxidation, a TS-1 catalyst was used. TS-1 exhibited an MFI structure as pure silicalite-1, and the particle size ranged from 200 to 300 nm (Fig. 2g and Supplementary Fig. 7). Its Si/Ti molar ratio was 100 and its Brunauer–Emmett–Teller surface area and pore volume were 488 $m^2\ g^{-1}$ and 0.48 $cm^3\ g^{-1}$, respectively (Supplementary Table 1 and Supplementary Fig. 8). Isomorphic substitution of Ti in a zeolite framework was confirmed using diffuse reflectance ultraviolet–visible (UV–vis) spectroscopy, infrared spectroscopy and Raman spectroscopy techniques (Fig. 2h and Supplementary Fig. 9). On TS-1, an absorption band below 250 nm in the UV–vis diffuse reflectance spectra was characteristic of the isomorphic Ti substitution, and there was no extra-framework TiO_2, as evidenced by the absence of an absorption band near 270– 330 nm (ref. [11,23]). On the contrary, there was no absorption band on silicalite-1. A vibrational band at 960 cm^{-1} in the Fourier transform infrared spectra of TS-1 was attributed to Si–O–Ti bonds in the framework[24]. The Raman spectral profiles of both silicalite-1 and TS-1 showed Raman bands resembling the MFI structure at 299 and 380 cm^{-1} (ref. [25]). The increase in the band at 970 cm^{-1} and the absence of Raman bands (TiO_2 on TS-1) support the isomorphic substitution of the Ti species.

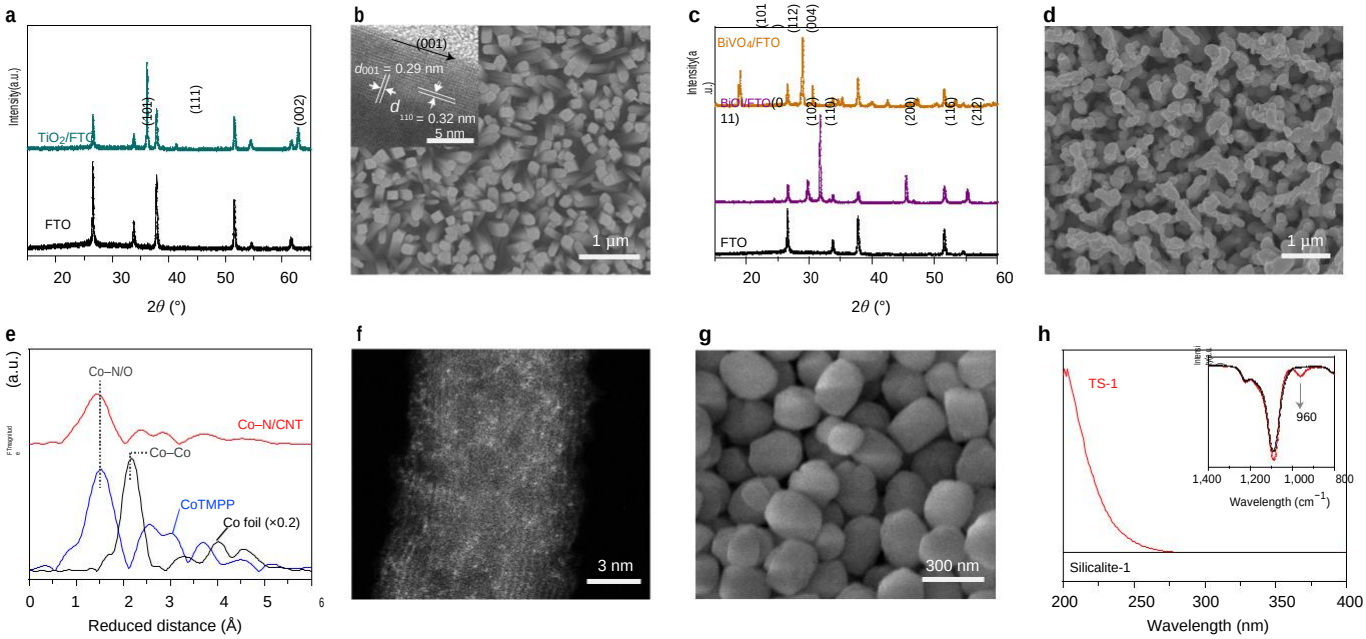

Fig. 2 | Catalyst characterization. a, X-ray diffraction patterns of TiO_2/FTO and FTO. **b**, SEM and HR-TEM (inset) images of TiO_2 photoanode. **c**, X-ray diffraction patterns of $BiVO_4$/FTO, BiOI/FTO and FTO. **d**, SEM image of the CoPi/$BiVO_4$ photoanode. **e**, EXAFS spectra of Co–N/CNT, CoTMPP and Co foil. **f**, HAADF-STEM image of Co–N/CNT. **g**, SEM image of TS-1. **h**, UV–vis diffuse reflectance spectra and Fourier transform infrared spectral profiles (inset) of TS-1 and silicalite-1.

Propylene epoxidation using the integrated catalytic system. Photocatalytic activity measurements of TiO_2 were carried out using a photo-electrochemical cell with a three-electrode configuration. Under sunlight illumination, the photocurrent density of the TiO_2 photoanode for water oxidation at 1.23 V versus a reversible hydrogen electrode (RHE) was 1.15 mA cm^{-2} with the onset potential of 0.4 V (versus RHE) in an Ar-saturated 0.1 M sodium phosphate (NaPi) buffer at pH 6 (Fig. 3a), and it showed a stable photocurrent for 24 h (Supplementary Fig. 10a). Because the TiO_2 photoanode is stable regardless of the electrolyte's pH, it showed an almost similar photocurrent in a wide range of pHs, allowing for its use with electrolytes with a broad range of pH values (Supplementary Fig. 10b).

The electrocatalytic activity and selectivity of the Co–N/CNT catalyst for H_2O_2 production were investigated in a 0.1 M NaPi buffer using a rotating ring-disc electrode (RRDE) technique. The oxygen reduction reaction (ORR) polarization curve shows that the Co–N/CNT catalyst began generating the H_2O_2 production current from 0.75 V (versus RHE) in the O_2-saturated 0.1 M NaPi buffer at pH 6 (Fig. 3b). RRDE and Koutecky–Levich analyses indicated the consistently high H_2O_2 selectivity (70–80%) of the Co–N/CNT catalyst (Fig. 3b and Supplementary Fig. 11). The Co–N/CNT catalyst was also active for electrochemical H_2O_2 production under various pH conditions (pH 2–8), extending the potential applicability of this catalyst for use with other photoanodes (Supplementary Fig. 12). In particular, even in an acidic electrolyte, where the dissolution of metal species or the oxidation of carbon surfaces is prominent[26], the Co−N/CNT catalyst exhibited a constant current and high selectivity for H_2O_2 production. We assessed the long-term durability of the Co−N/CNT catalyst by potential cycling in the range of 0.6–1.0 V and at a scan rate of 50 mV s^{-1} in an O_2-saturated 0.1 M NaPi buffer solution. After the durability test, high peroxide current density and selectivity for H_2O_2 production were maintained, demonstrating the catalyst's excellent stability (Supplementary Fig. 13). Furthermore, bright-field STEM (BF-STEM) and HAADF-STEM images of Co–N/CNT before and after the durability test were nearly the same, indicating that atomically dispersed Co species were not agglomerated or detached from the CNT support (Supplementary Fig. 14).

Next, a TiO_2 photoanode and a piece of carbon paper coated with a Co–N/CNT catalyst as a cathode were prepared for the photo-electrochemical H_2O_2 production. Bias-free photo-electrochemical H_2O_2 production occurs when an inter-section exists in the linear sweep voltammetry (LSV) curves of a photoanode and cathode. The predicted operating current of the integrated photo-electrochemical cell was 1.36 mA at 0.51 V (versus RHE), as shown in Fig. 3c. Actual bias-free photo-electrochemical H_2O_2 production was performed by connecting the TiO_2 photo-anode (in Ar-saturated 0.1 M NaPi buffer) and Co–N/CNT cathode (in O_2-saturated 0.1 M NaPi buffer) using alligator clips and copper wire as an external circuit. To verify the photo-electrochemical H_2O_2 production, the amount of H_2O_2 was estimated as a function of time using a colorimetric method with *N*,*N*-diethyl-*p*-phenylenediamine (DPD)[22,27]. We observed the continuous production of H_2O_2 over 5 h of reaction. Leaching of Co–N/CNT in the buffer solution could not be detected (Supplementary Table 2), confirming that it can con-tinuously and stably supply H_2O_2 for propylene epoxidation by TS-1 (Fig. 3d).

Propylene epoxidation was performed using photo-electrochemically produced H_2O_2 in a 0.1 M NaPi buffer at pH 6, in which TS-1 was dispersed in a cathodic electrolyte with the supply of propylene and O_2. As shown in Fig. 3e, PO was simultane-ously produced with H_2O_2 generation, and its production increased linearly with time. The remaining H_2O_2 was nearly constant after 1 h, which indicates that the generated H_2O_2 was promptly consumed by propylene epoxidation. Initial H_2O_2 utilization efficiencies (1 and 2 h) were low due to PO adsorption on TS-1 (Supplementary Fig. 15). However, after the passage of 3 h, the sum of the PO production and remaining H_2O_2 matched well with the amount of H_2O_2 production in the absence of TS-1, showing 97% H_2O_2 utilization (Fig. 3d,e and Supplementary Fig. 16). The catalytic system exhibited steady PO production for 24 h (total, 205 μmol; Fig. 3e inset). It is

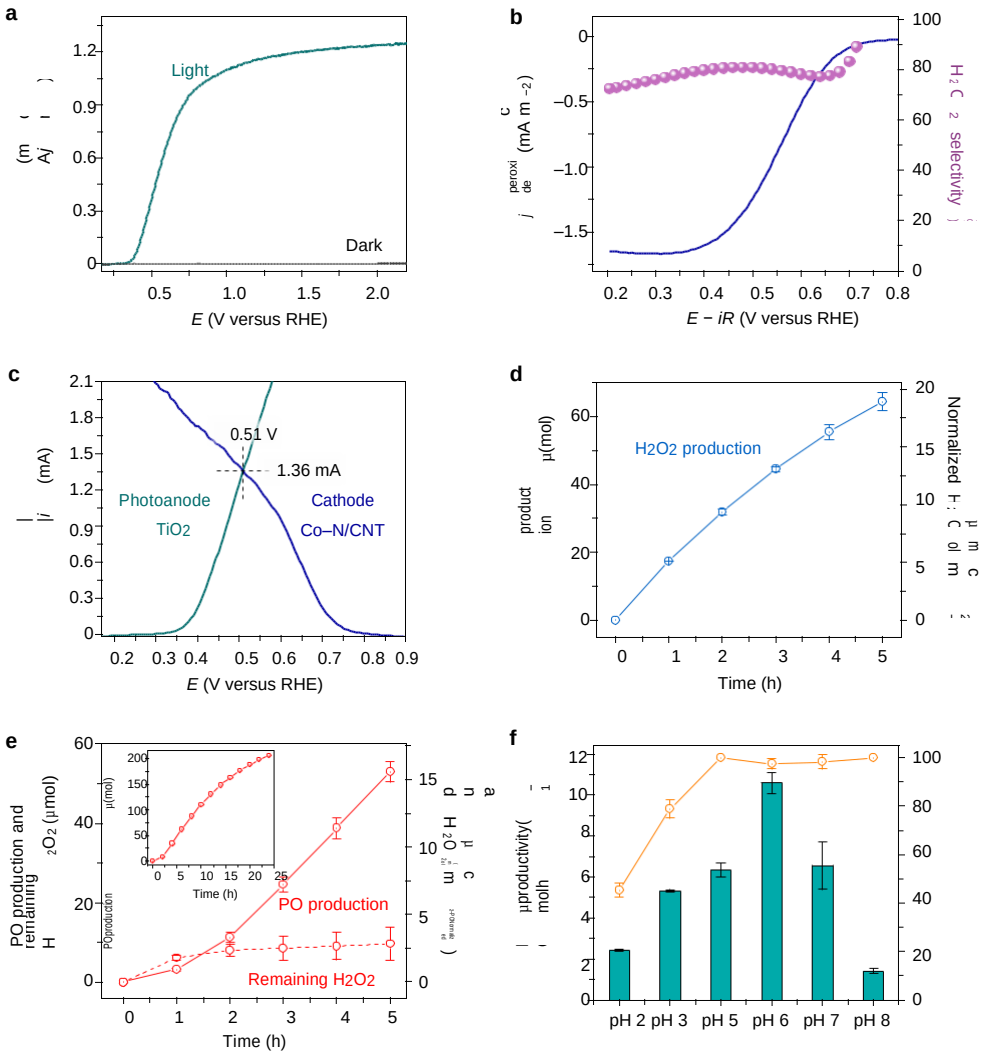

Fig. 3 | H_2O_2 production and propylene epoxidation in the integrated catalytic system. a, Photocurrent density (*j*) of TiO_2 photoanode under simulated solar light irradiation and dark conditions in an Ar-saturated 0.1 M NaPi buffer at pH 6. *E*, potential. **b**, LSV curves and H_2O_2 selectivity of the Co–N/ CNT catalyst in an O_2-saturated 0.1 M NaPi buffer at pH 6. $j_{peroxide}$, current density of peroxide. **c**, Overlap of the LSV curves of the TiO_2 photoanode and Co–N/CNT cathode on carbon paper in Ar- and O_2-saturated 0.1 M NaPi buffers at pH 6. **d**, H_2O_2 production during the photo-electrochemical (TiO_2 photoanode and Co–N/CNT cathode) reaction in a 0.1 M NaPi buffer at pH 6. **e**, PO production and remaining H_2O_2 during the reactions in photo-electro-heterogeneous catalytic system in a 0.1 M NaPi buffer at pH 6. Inset: PO production for 24 h. **f**, PO production rate and PO selectivity after 5 h of reaction in solutions with different pH values. All light was simulated as one sun (AM 1.5G) of illumination. The error bars indicate the standard deviation based on at least three independent measurements.

notable that O_2 was the only oxidizing agent in the overall reaction (C_3H_6 + 0.5 O_2 →C_3H_6O). Propylene epoxidation was performed at various pH values, and the production rate of PO was found to be the highest at pH 6 (10.6 μmol h^{-1}) with 97.5% PO selectivity (Fig. 3f and Supplementary Fig. 17). As the pH decreased from pH 6, the produc-tion rates of both H_2O_2 and PO declined (Supplementary Figs. 17–20 and Fig. 3f). In an acidic buffer, PG was formed due to the hydroly-sis of PO (Fig. 3f and Supplementary Fig. 17b), resulting in low PO selectivity (~45% PO selectivity at pH 2)[28]. At pH values of 7 and 8, PO selectivity was over 98%, but the PO production decreased, which may be attributed to the inhibition of propylene epoxidation on TS-1 by alkali metals in the buffer solutions (Fig. 3f)[29]. In this catalytic system, most PO was detected in the gaseous phase due to its high vapour pressure and continuous purging by O_2 and propyl-ene; less than 5% of all PO remained in the liquid phase based on the total PO production after 5 h. At low pH values, PG was detected in the liquid phase because of its low vapour pressure. There were no other detectable by-products. In the absence of the TS-1 catalyst, PO and by-products were not produced, demonstrating that the TS-1 catalyst was essential for propylene epoxidation (Supplementary Fig. 21). Furthermore, additional control experiments clearly showed that propylene was neither reduced on the Co–N/CNT cath-ode (Supplementary Fig. 22) nor directly oxidized to PO by O_2 in the absence of H_2O_2 (produced). The H_2O_2 production rate was the most important factor that determined the overall performance of PO production (Supplementary Fig. 23).

Propylene epoxidation under visible light illumination. We employed a TiO_2 semiconductor as a photoanode to observe the effects of pH on propylene epoxidation via a photo-electro-heterogeneous catalytic system because TiO_2 photoanodes are stable across a wide range of electrolyte pH values. However, a TiO_2 photoanode can utilize only UV light, which is <5% of the full sunlight spectrum, because of its large bandgap (3.1−3.3 eV)[30,31]. This limits the effective

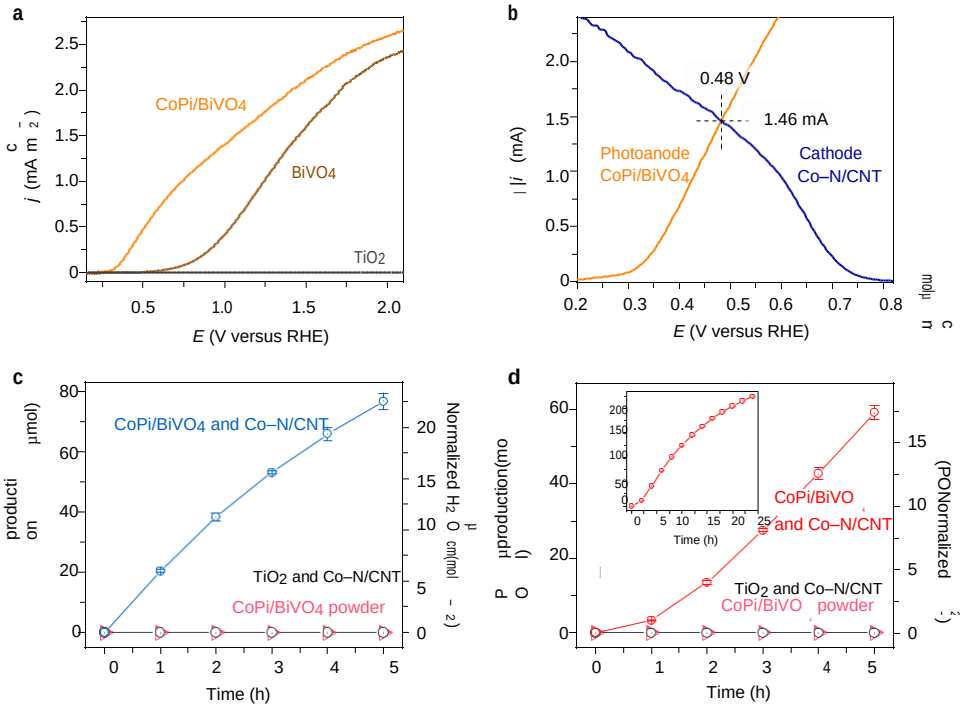

Fig. 4 | H_2O_2 and PO production in the integrated catalytic system under visible light. a, Photocurrent density of CoPi/$BiVO_4$, $BiVO_4$ and TiO_2 photoanodes in an Ar-saturated 0.1 M NaPi buffer at pH 6 under visible light (λ > 420 nm) illumination. **b**, Overlap of the LSV curves of the CoPi/ $BiVO_4$ photoanode and Co–N/CNT on carbon paper in Ar- and O_2-saturated 0.1 M NaPi buffers at pH 6, respectively. **c**, H_2O_2 production during the photo-electrochemical and photocatalytic reaction in a 0.1 M NaPi buffer at pH 6. **d**, PO production in the presence of photo-electro-heterogeneous catalytic and photo-heterogeneous catalytic systems in a 0.1 M NaPi buffer at pH 6. Inset: PO production for 24 h. The light intensity was 160 mW cm^{-2}, with a 420 nm cut-off filter. The error bars indicate the standard deviation based on three independent measurements.

use of sunlight to drive water oxidation. By contrast, a $BiVO_4$ photo-anode can utilize the visible light region, owing to its suitable band-gap of 2.4–2.6 eV (refs. [20,32]). Hence, we applied a $BiVO_4$ film as a photoanode to produce PO under visible light. The LSV curve of the $BiVO_4$ photoanode for water oxidation under visible light (wave-length, λ >420 nm) showed a 0.96 mA cm^{-2} photocurrent density at 1.23 V (versus RHE), while a negligible TiO_2 photoanode photocur-rent was observed (Fig. 4a). After the photo-electrodeposition of CoPi on $BiVO_4$, the current density of the CoPi/$BiVO_4$ photoanode increased to 1.73 mA cm^{-2} at 1.23 V (versus RHE), as compared with that of bare $BiVO_4$, with an onset potential shift of 0.25 V in the negative direction (Fig. 4a). The CoPi cocatalyst loading helped the efficient charge transfer between $BiVO_4$ and water by withdrawing the generated hole and retarding the charge recombination process on the surface of $BiVO_4$ (ref. [20]). The incident photon-to-current conversion efficiency (IPCE) further confirmed that TiO_2 was only active in the range of UV light, whereas $BiVO_4$ and CoPi/$BiVO_4$ were active up to a wavelength of 520 nm (Supplementary Fig. 24). For comparison, the LSV curves of CoPi/$BiVO_4$, bare $BiVO_4$ and TiO_2 photoanodes under simulated solar light irradiation are shown in Supplementary Fig. 25. The macroporous CoPi/$BiVO_4$ exhibited a higher photocurrent density when compared to a TiO_2 photo-anode of the same size, although we utilized a large active area of the CoPi/$BiVO_4$ film (active area, 3.4 cm^2), which typically shows higher photocurrent densities over small active areas (<0.5 cm^2)[32,33].

When the CoPi/$BiVO_4$ photoanode was integrated with the Co–N/CNT cathode for photo-electrochemical H_2O_2 production under visible light (λ > 420 nm), the intersection point was 1.46 mA at 0.48 V (versus RHE; Fig. 4b). It generated a total of 76.7 µmol of H_2O_2 over 5 h in a 0.1 M NaPi buffer at pH 6, while no H_2O_2 pro-duction was observed when the TiO_2 photoanode was used due to its large bandgap (Fig. 4c). The apparent quantum yield for H_2O_2 production for TiO_2 was approximately 0% at 450 nm, while that for CoPi/$BiVO_4$ was 5.25% (Supplementary Fig. 26). Additionally, an H_2O_2 production experiment was performed using powder-type TiO_2, $BiVO_4$ and CoPi/$BiVO_4$ photocatalysts to compare the photo-electrochemical and powder-type photocatalytic systems. None of the powder-type photocatalysts could produce H_2O_2 in the absence of a sacrificial agent, suggesting that the integrated photo-electrochemical system is essential for bias-free H_2O_2 pro-duction (Fig. 4c and Supplementary Fig. 27).

We next performed propylene epoxidation over TS-1 using photo-electrochemically produced H_2O_2 from a CoPi/$BiVO_4$ pho-toanode and Co–N/CNT cathode under visible light (λ >420 nm). The stable and continuous production of PO was observed for 5 h of reaction, with a production rate of 11.8 µmol h^{-1} (Fig. 4d). Moreover, the amount of H_2O_2 produced in the absence of TS-1 (based on the sum of the PO production and remaining H_2O_2) indi-cated 94% of H_2O_2 utilization, although low H_2O_2 utilization effi-ciencies at 1 and 2 h were observed, which could be attributed to PO absorption on TS-1 (as described previously; Supplementary Figs. 15, 28 and 29). A steady production was achieved for 24 h, yielding a total of 224 µmol of PO with high PO selectivity over 99% (Fig. 4d inset and Supplementary Table 3). Although this PO production rate is relatively low compared with those obtained in other works (Supplementary Table 4), it can be improved substan-tially by increasing the H_2O_2 production rate, as described above. These results indicate that our photo-electro-heterogeneous cata-lytic system could also stably produce PO under visible light irra-diation, suggesting that it has potential applications in commercial light-emitting diode bulbs and under ambient sunlight. By contrast, PO was not produced when the TiO_2 photoanode and CoPi/$BiVO_4$

powder-type photocatalyst were used because they could not pro-duce H_2O_2 under visible light and without the help of a sacrificial agent, respectively (Fig. 4d). When the TiO_2, $BiVO_4$ and CoPi/$BiVO_4$ photoanodes were applied to the system under simulated solar light irradiation, the highest PO productivity was exhibited by the CoPi/$BiVO_4$ photoanode, followed by the TiO_2 and $BiVO_4$ photoanodes (Supplementary Fig. 30 and Supplementary Table 3). The trend was consistent with the order of H_2O_2 productivity (Supplementary Fig. 31). We note that this work presents a proof-of-concept inte-grated photo-electro-heterogeneous catalytic system for PO production using in situ-generated H_2O_2, and this system is not profitable with the current PO productivity. However, a prelimi-nary techno-economic analysis of our system showed possibilities of its practical use, when the solar-to-H_2O_2 conversion efficiency is increased and the system is scaled up (Supplementary Note 1, Supplementary Tables 5 and 6 and Supplementary Fig. 32).

Conclusions

This study demonstrates that the developed photo-electro-heterogeneous catalytic system can successfully produce PO from propylene and O_2. With a TiO_2 photoanode, it showed the highest PO production rate (10.6 μmol h^{-1} for 5 h) and 97.5% PO selectivity at pH 6 under simulated solar light. This system stably produced 205 μmol of PO with high selectivity (98%) for 24 h. Moreover, it could also operate under visible light illumination with a CoPi/ $BiVO_4$ photoanode, showing stable and continuous PO production up to 224 μmol for 24 h with PO selectivity over 99%. This integrated system has great advantages in that it uses O_2 instead of expensive reagents (for example, H_2 or H_2O_2) and its overall reactions take place in a single, environmentally friendly system without the use of any additional bias or sacrificial agents. For the practical viabil-ity of this integrated catalytic system, the rate of PO production should be much improved. As the PO productivity on a heteroge-neous catalyst is primarily governed by the photo-electrochemical H_2O_2 production rate, we need to focus on improving the perfor-mances of photocatalysts and electrocatalysts. We should also focus on developing a more efficient H_2O_2 production system (for exam-ple, a gas diffusion electrode system where the problem of low O_2 solubility in an aqueous solution can be addressed) and optimize the performance of heterogeneous catalysts. We believe that this photo-electro-heterogeneous catalytic system provides a more sus-tainable way of producing PO with O_2 beyond the currently available methods of PO production and should broaden the applicability of the photo-electrochemical system in the chemical industry.

Methods

Photocatalyst synthesis. A rutile TiO_2 nanowire film was hydrothermally grown on a FTO substrate[16,17]. First, 15 ml of hydrochloric acid (35%, Samchun Chemical) was diluted with 15 ml of deionized water and mixed with 0.5 ml of titanium(IV) butoxide (97%, MilliporeSigma). This clear solution was transferred to a Teflon-lined stainless-steel autoclave (125 ml), and the FTO substrate was submerged in the solution. The sealed autoclave was kept in an oven at 150 °C for 5 h and then cooled to room temperature slowly. After rinsing and drying, the sample was annealed at 550 °C for 5 h to increase crystallinity.

A macroporous $BiVO_4$ film was prepared according to a previously reported method[19]. Briefly, three solutions for synthesizing $BiVO_4$ were prepared. First, a bismuth nitrate solution was prepared by dissolving 0.04 M of bismuth nitrate pentahydrate (≥99.99%, MilliporeSigma) in 0.4 M (50 ml) of a potassium iodide solution (99%, FujiFilm Wako Chemicals). The pH of this solution was then reduced to 1.7 by adding HNO_3 (60%, Junsei Chemical). The second solution consisted of 0.23 M of 1,4-benzoquinone (≥98%, MilliporeSigma) in absolute ethanol (20 ml). Later, both solutions were mixed to obtain a dark brown BiOI precursor solution. A dark orange BiOI layer was electrodeposited on the FTO by applying a constant potential of –0.1 V against Ag/AgCl (RE-1B, ALS) for 420 s. Next, 0.4 M vanadyl acetylacetonate (98%, MilliporeSigma) in dimethyl sulfoxide (99%, Kanto Chemical) was prepared for converting the BiOI to $BiVO_4$. This solution was uniformly drop-cast on the BiOI layer, and then the film was annealed at 450 °C for 2 h. Finally, a brownish crust was removed from the samples by washing with 1 M NaOH (98%, Alfa Aesar) for 30 min, and CoPi was applied onto the $BiVO_4$ photoanode via photo-assisted electrodeposition[21]. A three-electrode cell was used with the $BiVO_4$ working electrode (one sun position), Ag/AgCl reference electrode and a Pt mesh counter electrode, and CoPi was deposited for 6 min at ~0.2−0.3 V (versus RHE) with photocurrent densities of ~1−4 μA cm^{-2} in a 0.1 M potassium phosphate buffer at pH 6.7 and containing 0.5 mM of cobalt nitrate (98%, Alfa Aesar).

Powder samples of TiO_2, $BiVO_4$ and CoPi/$BiVO_4$ could be obtained by scratching the corresponding film.

Electrocatalyst synthesis. Synthesis of Co–N/CNT, employing CoTMPP as the Co and N precursors, was conducted following a silica coating-mediated process with some modifications[22]; 0.28 g of CoTMPP was ground in a mortar for 5 min, and the resulting fine powder was mixed with 0.2 g of acid-treated CNT for 10 min. The CoTMPP–CNT mixture was heated to 400 °C at a ramping rate of 2 °C min^{-1} and maintained at 400 °C for 3 h under N_2 gas (99.999%) at a flow rate of 1 l min^{-1}. The resulting composite was mixed with 1.0 ml of tetraethyl orthosilicate in a mortar, followed by mixing with 1.0 ml of formic acid. The paste-like mixture was kept at room temperature for 12 h in a fume hood, then heated to 900 °C at a ramping rate of 2 °C min^{-1} and maintained at that temperature for 3 h. To etch the silica, the pyrolysed composite was mixed with 1:1 (v/v) of ethanol/10%-aqueous-HF solution. The slurry was stirred for 30 min, filtered and washed with ethanol several times. Finally, the HF etching process was repeated in the same manner, and the product was oven-dried at 60 °C.

Characterization of photocatalysts and electrocatalysts. The X-ray diffraction patterns of photoanode films and Co–N/CNT catalysts were recorded using an X'Pert PRO diffractometer (Malvern Pananalytical) with Cu Kα radiation (λ =1.5406 Å) and a high-power X-ray diffractometer (D/Max2500V/PC, Rigaku) with Cu Kα radiation, respectively, in the diffraction angle (2θ) range of 10–70°. The TEM (HR-TEM, HAADF-STEM and BF-STEM) and SEM images were obtained using a JEM-2100F microscope (JEOL) and a SU8220 microscope (Hitachi High-Technologies), respectively. The optical properties were determined by UV–vis diffuse reflectance spectroscopy using a UV-3600 (Shimadzu). The XPS measurements were performed with a K-Alpha X-ray photoelectron spectrometer (Thermo Fisher Scientific) with a monochromatic Al Kα X-ray source. The N_2 sorption isotherm was recorded using a Belsorp-Max (MicrotracBEL) system. The Co content in the Co–N/CNT catalyst was quantified using an inductively coupled plasma optical emission spectrometer (700-ES, Varian). X-ray absorption spectroscopy (XAS) was performed at beamline 10D of the Pohang Accelerator Laboratory. The storage ring was operated at an energy of 3 GeV and a beam current of 300 mA. The incident photons were monochromated by Si(111) double crystal, detuned by 30% to remove high-order spectral contamination and calibrated using a standard Co foil. Co–N/CNT and CoTMPP powders were pressed using a hand-held pelletizer for XAS measurements. XAS spectra were obtained in transmission detection mode. The resulting XAS data were treated using the Athena program to remove the background and for normalization[34].

Electrochemical measurements. Electrochemical measurements were conducted using an electrochemical workstation (CHI760E, CH Instruments). The three-electrode system was constructed using a graphite rod counter electrode, an Ag/AgCl reference electrode and a catalyst-loaded RRDE (AFE7R9GCPT, Pine Research Instrumentation). The potential was converted to a RHE scale. For the RHE conversion, a two-electrode system was built with a Pt coil and reference electrode immersed in an electrolyte with H_2 bubbling. The Pt coil acted as the RHE at which the H^+/H_2 equilibrium was established. With continuous H_2 bubbling, the open circuit voltage was monitored until a stable open circuit voltage value was observed. Before every electrochemical measurement, the RRDE surface was cleaned by successively polishing it with a 1 μm alumina (Allied High Tech Products) aqueous suspension and 0.3μm alumina (Allied High Tech Products) aqueous suspension, and was then subjected to ultrasonication in deionized water. The Co–N/CNT catalyst ink was prepared by mixing 5mg of catalyst, 50μl of deionized water, 12.5μl of Nafion dispersion (5wt%, D521, Dupont de Nemours) and 537μl of anhydrous ethanol. The catalyst ink was homogenized using an ultrasonic bath. Then, 6μl of the ink was deposited onto the RRDE disc. The resulting catalyst loading was 0.2mgcm^{-2}. After soaking the catalyst-loaded RRDE in a N_2-saturated electrolyte, cyclic voltammetry was performed between 0.05 and 1.20V (versus RHE) at a scan rate of 100mVs^{-1}. Steady cyclic voltammetry responses were observed within 20 cycles. The Pt ring of the RRDE was electrochemically cleaned in the same potential range with a scan rate of 500mVs^{-1} for 50 cycles. The electrochemical impedance spectroscopy experiments were conducted at 0.68V (versus RHE) from 100,000 to 1Hertz at an electrode rotation speed of 1,600r.p.m. in an O_2-saturated electrolyte (Supplementary Fig. 33). The series resistance was determined at the high-frequency tail of the Nyquist plot for iR (potential drop; i, current; R, resistance) compensation. The ORR polarization curve was obtained by LSV from 1.2 to 0.2V (versus RHE) at a scan rate of 5mVs^{-1} and electrode rotation speeds of 2,025, 1,600, 1,225 and 900r.p.m. for Koutecky– Levich analysis (equation (1)). To correct the non-Faradaic current (capacitive current) from the LSV curve, the same measurements were made in an N_2-saturated electrolyte.

$$\frac{1}{j} = \frac{1}{j_k} + \frac{1}{0.62nFAD_O^{2/3}\nu^{-1/6}C_O\omega^{1/2}} = \frac{1}{j_k} + \frac{1}{B\times\omega^{1/2}} \quad (1)$$

In equation (1), i, i_K, n, F, A, D_O, ν, C_O and ω represent the measured current, kinetic current, electron transfer number, Faraday constant (96,485 C mol^{-1}), electrode area, diffusion coefficient of O_2, kinematic viscosity, O_2 concentration and electrode rotation speed, respectively. The plot of i^{-1} as a function of $\omega^{-1/2}$ yields a line with a slope of B^{-1}, which was used to calculate n. The D_O, ν and C_O values in a 0.1 M NaPi electrolyte are 8.90 ×10^{-6} cm^2 s^{-1}, 0.0111 cm^2 s^{-1} and 1.21 ×10^{-6} mol cm^{-3}, respectively[35–37].

To measure the H_2O_2 yield, the Pt ring potential was maintained at 1.3 V (versus RHE) during the LSV measurements, and the H_2O_2 selectivity was calculated according to the following equation:

$$H_2O_2 \text{ selectivity } (\%) = \frac{200}{1 + \frac{N \times i_d}{i_r}} \quad (2)$$

where i_d, i_r and N indicate the disc current, ring current and collection efficiency (37%, provided by the manufacturer), respectively. To assess the durability of the catalysts, potential cycling tests were performed between 0.6 and 1.0 V (versus RHE) with an electrode rotation of 1,600 r.p.m. and a scan rate of 50 mV s^{-1} for 1,000 cycles in the O_2-saturated electrolyte. After cycling, the ORR activity was measured in a fresh electrolyte.

Photo-electrochemical measurements of photoanode and cathode. The LSV curves of the photoanodes were measured using a digital multimeter (Ivium-n-Stat Multichannel potentiostat, Ivium Technologies) with an Ag/AgCl reference electrode and a Pt wire counter electrode in an Ar-saturated 0.1 M NaPi solution from 0–2 V (versus RHE) and at a scan rate of 10 mV s^{-1}. The photoanode (3.4 cm^2) was illuminated using a 300 W Xe arc lamp (66902, Newport) with an air mass 1.5 global (AM 1.5G) filter at 100 mW cm^{-2} under one sun of simulated illumination. For visible light illumination, the intensity was adjusted to 160 mW cm^{-2} with a 420 nm cut-off filter. The light intensity was adjusted using a standard Si cell (PEC-SI01, Peccell Technologies). The IPCE spectra were recorded using a 300 W Xe arc lamp (66902, Newport) equipped with a monochromator (CS260, Newport). The LSV curves of the Co–N/CNT cathode (geometric area, 3.74 cm^2) were also measured from 1.2 to 0.05 V (versus RHE) at a scan rate of 5 mV s^{-1} in an O_2-saturated 0.1 M NaPi solution at pH 6.

TS-1 synthesis. We synthesized TS-1 as previously reported in the literature[38]; 2 g of Tween 20 (MilliporeSigma) was added to 21 ml of deionized water, and this solution was added to 30.3 g of a tetrapropylammonium hydroxide (TPAOH) solution (1 M in water, MilliporeSigma) dropwise with stirring. To this mixed solution, 36 g of tetraethyl orthosilicate (≥99.0%, MilliporeSigma) was added dropwise with stirring. After 1 h of stirring, 0.61 g of titanium(IV) butoxide (97%, MilliporeSigma) in 9.12 g of isopropyl alcohol (≥99.5%, Daejung Chemicals and Metals) was added dropwise. The molar ratio of the synthesis gel was 1 SiO_2:0.01 TiO_2:0.17 TPAOH:14.5 H_2O:0.009 Tween 20:0.88 isopropyl alcohol. After stirring for another 1 h, the resulting solution was transferred into a Teflon-lined stainless-steel autoclave and heated at 150 °C for 20 h. The precipitates were separated by centrifugation, washed with water several times and dried at 110 °C overnight. The synthesized sample was calcined in a muffle furnace at 550 °C for 15 h. Silicalite-1 was synthesized with the same procedure as described above, without titanium(IV) butoxide.

TS-1 characterization. The X-ray diffraction patterns of TS-1 and silicalite-1 were recorded on a high-resolution X-ray diffractometer (SmartLab, Rigaku) using Cu Kα radiation in the 2θ range of 5–50°, at a scanning speed of 5° min^{-1}. The N_2 sorption isotherm was performed using Belsorp-Max II (MicrotracBEL). The SEM analysis was performed using an SU8220 instrument (Hitachi High-Technologies) at 5 kV. UV–vis diffuse reflectance and infrared spectra were recorded on a Cary 5000 instrument (Agilent Technologies) and Varian 670/620 infrared spectrometer (Varian), respectively. Raman spectra were recorded on an alpha300R Micro-imaging Raman Spectrometer (WITec) equipped with a 532 nm Nd/yttrium-aluminium-garnet excitation laser and electrically cooled CCD (charge-coupled device) detector. A spectrometer with a grating of 1,800 grooves mm^{-1} was used.

Hydrogen peroxide detection. The amount of H_2O_2 was estimated using the DPD method[27]. First, DPD and peroxidase solutions were prepared by dissolving 0.05 g DPD (≥98.0%, MilliporeSigma) in 5 ml of 0.1 N H_2SO_4 and 5 mg of peroxidase from horseradish (MilliporeSigma) in 5 ml of deionized water, respectively. These solutions were kept at 5 °C. Next, 2.7 ml of a 0.1 M NaPi buffer (pH 6.0), 0.05 ml of DPD solution, 0.05 ml of peroxidase solution and 0.2 ml of sample were mixed. The absorbance of the mixed solution at λ =551 nm was measured using a UV-2600 instrument (Shimadzu). The amount of H_2O_2 was calculated from an external standard curve (coefficient of determination, R^2 >0.99).

Propylene epoxidation and product analysis. The overall reaction was performed in a single reactor composed of an anode cell and a cathode cell. The anode cell was separated from the cathode cell through a 0.18-mm-thick Nafion membrane (Nafion 117, MilliporeSigma), and a 0.1 M NaPi solution (pH 2−8) was used as the electrolyte. The anode and cathode cells consisted of a photoanode (3.4 cm^2) with 28 ml electrolyte and a Co–N/CNT cathode (geometric area, 3.74 cm^2) with TS-1 (5 mg ml^{-1}) in a 9 ml electrolyte, respectively. The photoanode and cathode were connected with alligator clips and copper wire as an external circuit.

In the photocatalytic powder system, the powder-type photocatalyst (2.5 mg ml^{-1}) and TS-1 (5 mg ml^{-1}) were added together in a 5 ml electrolyte in a single cell. The photoanode (or powder-type photocatalyst) was illuminated using a 300 W Xe arc lamp (66902 Newport) with an AM 1.5G filter at 100 mW cm^{-2} under one sun of illumination. For visible light illumination, the intensity was adjusted to 160 mW cm^{-2} with a 420 nm cut-off filter. Argon gas was continuously bubbled into the anode electrolyte, and O_2 and C_3H_6 gas were continuously bubbled into the cathode electrolyte from 20 min before the reaction until the reaction was completed. During the reactions, the outlet gases were periodically analysed via gas chromatography (7820A, Agilent Technologies) equipped with an HP–FFAP column (30 m ×530 μm ×1.00 μm) and flame-ionization detector. For liquid analysis, the sample was filtered using a 0.45 μm hydrophilic syringe filter (13HP045AN, Advantec MFS). Then, it was injected into the inlet of the gas chromatography instrument equipped with an HP-5 (30 m ×320 μm ×0.25 μm) column. The products were quantified based on the external standard curves (R^2 >0.98) of the respective compounds. Propylene oxide selectivity was calculated according to the following equation:

$$\text{PO selectivity } (\%) = \frac{n_{PO}}{n_{PO} + n_{PG}} \times 100, \quad (3)$$

where n_{PO} and n_{PG} indicate PO production and PG production, respectively.

To calculate the H_2O_2 utilization efficiency, H_2O_2 production was estimated based on the H_2O_2 production rate during the initial 3 h. Subsequently, H_2O_2 utilization at each time was calculated as follows:

$$H_2O_2 \text{ utilization efficiency } (\%) = \frac{r_{PO} + r_{PG}}{r_{H_2O_2} - r'_{H_2O_2}} \times 100, \quad (4)$$

where r_{PO}, r_{PG}, $r_{H_2O_2}$ and $r'_{H_2O_2}$ indicate produced PO, PG and H_2O_2 and remaining H_2O_2 (every hour; μmol h^{-1}), respectively.

The apparent quantum yield (AQY) for H_2O_2 production was calculated by the multiplication of IPCE of photocatalyst and H_2O_2 current ratio of the electrocatalyst from RRDE as follows:

$$\text{AQY } (\%) = \text{IPCE} \times \frac{i_r}{N \times i_d}. \quad (5)$$

IPCE was measured at intersecting voltage; i_d, i_r and N indicate the disc current, ring current and collection efficiency derived from RRDE, respectively.

Data availability

The experimental data in the main text and the Supplementary Information are available at https://doi.org/10.6084/m9.figshare.16936906.

Received: 22 December 2020; Accepted: 12 November 2021;
Published online: 30 December 2021

References

\1.\Zuwei, X., Ning, Z., Yu, S. & Kunlan, L. Reaction-controlled phase-transfer catalysis for propylene epoxidation to propylene oxide. *Science* **292**, 1139–1141 (2001).
\2.\Leow, W. R. et al. Chloride-mediated selective electrosynthesis of ethylene and propylene oxides at high current density. *Science* **368**, 1228–1233 (2020).
\3.\Zhan, C. et al. Critical roles of doping Cl on Cu_2O nanocrystals for direct epoxidation of propylene by molecular oxygen. *J. Am. Chem. Soc.* **142**, 14134–14141 (2020).
\4.\Teržan, J., Huš, M., Likozar, B. & Djinović, P. Propylene epoxidation using molecular oxygen over copper- and silver-based catalysts: a review. *ACS Catal.* **10**, 13415–13436 (2020).
\5.\Cavani, F. & Teles, J. H. Sustainability in catalytic oxidation: an alternative approach or a structural evolution? *ChemSusChem* **2**, 508–534 (2009).
\6.\Lei, Y. et al. Increased silver activity for direct propylene epoxidation via subnanometer size effects. *Science* **328**, 224–228 (2010).
\7.\Ghosh, S. et al. Selective oxidation of propylene to propylene oxide over silver-supported tungsten oxide nanostructure with molecular oxygen. *ACS Catal.* **4**, 2169–2174 (2014).
\8.\ Huang, J. et al. Propene epoxidation with dioxygen catalyzed by gold clusters. *Angew. Chem. Int. Ed.* **48**, 7862–7866 (2009).
\9.\Torres, D., Lopez, N., Illas, F. & Lambert, R. M. Low-basicity oxygen atoms: a key in the search for propylene epoxidation catalysts. *Angew. Chem. Int. Ed.* **46**, 2055–2058 (2007).
\10.\Barton, J. L. Electrification of the chemical industry. *Science* **368**, 1181–1182 (2020).
\11.\Gordon, C. P. et al. Efficient epoxidation over dinuclear sites in titanium silicalite-1. *Nature* **586**, 708–713 (2020).

\12.\Campos-Martin, J. M., Blanco-Brieva, G. & Fierro, J. L. G. Hydrogen peroxide synthesis: an outlook beyond the anthraquinone process. *Angew. Chem. Int. Ed.* **45**, 6962–6984 (2006).
\13.\Hayashi, T., Tanaka, K. & Haruta, M. Selective vapor-phase epoxidation of propylene over Au/TiO_2 catalysts in the presence of oxygen and hydrogen. *J. Catal.* **178**, 566–575 (1998).
\14.\Uphade, B. S., Akita, T., Nakamura, T. & Haruta, M. Vapor-phase epoxidation of propene using H_2 and O_2 over Au/Ti–MCM-48. *J. Catal.* **209**, 331–340 (2002).
\15.\Sinha, A. K., Seelan, S., Tsubota, S. & Haruta, M. A three-dimensional mesoporous titanosilicate support for gold nanoparticles: vapor-phase epoxidation of propene with high conversion. *Angew. Chem. Int. Ed.* **43**, 1546–1548 (2004).
\16.\Liu, B. & Aydil, E. S. Growth of oriented single-crystalline rutile TiO_2 nanorods on transparent conducting substrates for dye-sensitized solar cells. *J. Am. Chem. Soc.* **131**, 3985–3990 (2009).
\17.\Liu, C., Tang, J., Chen, H. M., Liu, B. & Yang, P. A fully integrated nanosystem of semiconductor nanowires for direct solar water splitting. *Nano Lett.* **13**, 2989–2992 (2013).
\18.\Wang, G. et al. Hydrogen-treated TiO_2 nanowire arrays for photoelectrochemical water splitting. *Nano Lett.* **11**, 3026–3033 (2011).
\19.\Kim, T. W. & Choi, K.-S. Nanoporous $BiVO_4$ photoanodes with dual-layer oxygen evolution catalysts for solar water splitting. *Science* **343**, 990–994 (2014).
\20.\Park, Y., McDonald, K. J. & Choi, K.-S. Progress in bismuth vanadate photoanodes for use in solar water oxidation. *Chem. Soc. Rev.* **42**, 2321–2337 (2013).
\21.\Zhong, D. K., Choi, S. & Gamelin, D. R. Near-complete suppression of surface recombination in solar photoelectrolysis by "Co-Pi" catalyst-modified W:$BiVO_4$. *J. Am. Chem. Soc.* **133**, 18370–18377 (2011).
\22.\Ko, M. et al. Unassisted solar lignin valorisation using a compartmented photo-electro-biochemical cell. *Nat. Commun.* **10**, 5123 (2019).
\23.\Blasco, T., Camblor, M. A., Corma, A. & Perez-Pariente, J. The state of Ti in titanoaluminosilicates isomorphous with zeolite *β*. *J. Am. Chem. Soc.* **115**, 11806–11813 (1993).
\24.\Fan, W. et al. Synthesis, crystallization mechanism, and catalytic properties of titanium-rich TS-1 free of extraframework titanium species. *J. Am. Chem. Soc.* **130**, 10150–10164 (2008).
\25.\Li, C. et al. UV resonance Raman spectroscopic identification of titanium atoms in the framework of TS-1 zeolite. *Angew. Chem. Int. Ed.* **38**, 2220–2222 (1999).
\26.\Möller, S. et al. Online monitoring of electrochemical carbon corrosion in alkaline electrolytes by differential electrochemical mass spectrometry. *Angew. Chem. Int. Ed.* **59**, 1585–1589 (2020).
\27.\Bader, H., Sturzenegger, V. & Hoigné, J. Photometric method for the determination of low concentrations of hydrogen peroxide by the peroxidase catalyzed oxidation of N,N-diethyl-*p*-phenylenediamine (DPD). *Water Res.* **22**, 1109–1115 (1988).
\28.\Li, B. et al. Hydration of epoxides on [Co^{III}(salen)] encapsulated in silica-based nanoreactors. *Angew. Chem. Int. Ed.* **51**, 11517–11521 (2012).
\29.\Khouw, C. B. & Davis, M. E. Catalytic activity of titanium silicates synthesized in the presence of alkali-metal and alkaline-earth ions. *J. Catal.* **151**, 77–86 (1995).
\30.\Linsebigler, A. L., Lu, G. & Yates, J. T. Photocatalysis on TiO_2 surfaces: principles, mechanisms, and selected results. *Chem. Rev.* **95**, 735–758 (1995).
\31.\Zhang, D. et al. Plasmonic electrically functionalized TiO_2 for high-performance organic solar cells. *Adv. Funct. Mater.* **23**, 4255–4261 (2013).
\32.\Lee, Y. W. et al. Unbiased biocatalytic solar-to-chemical conversion by FeOOH/$BiVO_4$/perovskite tandem structure. *Nat. Commun.* **9**, 4208 (2018).
\33.\Lee, D. K. & Choi, K.-S. Enhancing long-term photostability of $BiVO_4$ photoanodes for solar water splitting by tuning electrolyte composition. *Nat. Energy* **3**, 53–60 (2018).
\34.\Ravel, B. & Newville, M. ATHENA, ARTEMIS, HEPHAESTUS: data analysis for X-ray absorption spectroscopy using IFEFFIT. *J. Synchrotron Radiat.* **12**, 537–541 (2005).
\35.\Liu, X., Richtering, W. & Akolkar, R. Investigation of the kinetics and mass transport aspects of hydrogen evolution during electroless deposition of nickel–phosphorus. *J. Electrochem. Soc.* **164**, D498–D504 (2017).
\36.\Chenlo, F., Moreira, R., Pereira, G. & Vázquez, M. J. Viscosity of binary and ternary aqueous systems of NaH_2PO_4, Na_2HPO_4, Na_3PO_4, KH_2PO_4, K_2HPO_4, and K_3PO_4. *J. Chem. Eng. Data* **41**, 906–909 (1996).
\37.\Yin, G. & Zhang, J. *Rotating Electrode Methods and Oxygen Reduction Electrocatalysts* 1st edn (Elsevier, 2014).
\38.\Khomane, R. B., Kulkarni, B. D., Paraskar, A. & Sainkar, S. R. Synthesis, characterization and catalytic performance of titanium silicalite-1 prepared in micellar media. *Mater. Chem. Phys.* **76**, 99–103 (2002).

Acknowledgements

This work was supported by the National Research Foundation of Korea (NRF-2016R1A5A1009405 and NRF-2017R1A2B4007310 to J.H.K.; NRF-2017M1A2A2087630 to J.-W.J.; NRF-2019M3D1A1079306 and NRF-2021R1A2C2007495 to S.H.J.; and NRF-2020R1A6A3A13075849 to M.K.). J.-W.J. also acknowledges the POSCO Science Fellowship of the POSCO TJ Park Foundation.

Author contributions

J.H.K., J.-W.J. and S.H.J. proposed and directed the project. M.K., Y.K. and J.W. conceived and designed the experiments. B.L. and H.L. performed the techno-economic analysis of the designed system. M.K. and R.M. prepared the TiO_2 and $BiVO_4$ photocatalysts and measured their performances with S.W.H. and P.S.; Y.K. synthesized and characterized the TS-1 catalyst. J.W. prepared the Co–N/CNT electrocatalysts and measured their selectivity for H_2O_2 production. M.K. and Y.K. measured the performance of PO conversion. J.K. and H.Y.J. contributed to TEM analysis. M.K., Y.K., J.W., S.H.J., J.-W.J. and J.H.K. co-wrote the manuscript. All authors read and commented on the manuscript.

Competing interests

The authors declare no competing interests.

Additional information

Correspondence and requests for materials should be addressed to Sang Hoon Joo, Ji-Wook Jang or Ja Hun Kwak.